JOURNAL OF VIROLOGY, June 2007, p. 6356–6368 Vol. 81, No. 12
0022-538X/07/$08.00+0 doi:10.1128/JVI.02805-06

Murine Hepatitis Virus Replicase Protein nsp10 Is a Critical Regulator of Viral RNA Synthesis▽

Eric F. Donaldson,[1] Amy C. Sims,[2] Rachel L. Graham,[4,5] Mark R. Denison,[3,4,5] and Ralph S. Baric[1,2]*

Department of Microbiology and Immunology, School of Medicine,[1] and Department of Epidemiology, School of Public Health,[2] University of North Carolina, Chapel Hill, North Carolina, and Departments of Pediatrics[3] and Microbiology and Immunology,[4] and The Elizabeth B. Lamb Center for Pediatric Research,[5] Vanderbilt University Medical Center, Nashville, Tennessee

Received 19 December 2006/Accepted 21 March 2007

Coronavirus replication requires proteolytic processing of the large polyprotein encoded by ORF1a/ab into putative functional intermediates and eventually ~15 mature proteins. The C-terminal ORF1a protein nsp10 colocalizes with viral replication complexes, but its role in transcription/replication is not well defined. To investigate the role of nsp10 in coronavirus transcription/replication, alanine replacements were engineered into a murine hepatitis virus (MHV) infectious clone in place of conserved residues in predicted functional domains or charged amino acid pairs/triplets, and rescued viruses were analyzed for mutant phenotypes. Of the 16 engineered clones, 5 viable viruses were rescued, 3 mutant viruses generated no cytopathic effect but were competent to synthesize viral subgenomic RNAs, and 8 were not viable. All viable mutants showed reductions in growth kinetics and overall viral RNA synthesis, implicating nsp10 as being a cofactor in positive- or negative-strand synthesis. Viable mutant nsp10-E2 was compromised in its ability to process the nascent polyprotein, as processing intermediates were detected in cells infected with this virus that were not detectable in wild-type infections. Mapping the mutations onto the crystal structure of severe acute respiratory syndrome virus nsp10 identified a central core resistant to mutation. Mutations targeting residues in or near either zinc-binding finger generated nonviable phenotypes, demonstrating that both domains are essential to nsp10 function and MHV replication. All mutations resulting in viable phenotypes mapped to loops outside the central core and were characterized by a global decrease in RNA synthesis. These results demonstrate that nsp10 is a critical regulator of coronavirus RNA synthesis and may play an important role in polyprotein processing.

Coronaviruses (CoVs) have historically been associated with severe disease in important domestic animals and mild upper respiratory tract infections in humans (human CoV strains HCoV-229E and HCoV-OC43), rarely leading to severe disease (24). However, the rapid identification of a CoV as the etiological agent responsible for severe acute respiratory syndrome (SARS) redefined historic perceptions. SARS-CoV spread globally and infected over 8,000 people, with mortality rates of about 10% (49). More recent studies have identified human CoVs NL63 and HKU-1 as being important lower respiratory tract pathogens (25, 53). With ubiquitous populations of CoVs found in many animals, it is not surprising that several newly identified CoVs that likely emerged from zoonotic reservoirs over the past 20 years have been described. An understanding of the basic biology and pathogenesis of CoV infection is of urgent importance.

CoVs are the largest known RNA viruses encoding plus-sense, 5′-capped, and polyadenylated genomes of 27 to 31 kb in length. CoVs are classified as members of the order *Nidovirales*, family *Coronaviridae*, genus *Coronavirus*, and are divided into three groups based on serological and phylogenetic categorizations (14, 29). Group 1 consists of NL63, HCoV-229E, and transmissible gastroenteritis virus; group 3 is composed of infectious bronchitis virus; and group 2 CoVs include HCoV-OC43, HKU-1, bovine CoV, SARS-CoV, and murine hepatitis virus (MHV) (14). MHV is an extensively studied CoV, with strain MHV-A59 being well characterized in cell culture and mouse model systems (33). The close relationship of MHV to SARS-CoV makes MHV an ideal model for prototype studies of the biology and pathogenesis of CoV infections in humans.

The first ~22 kb of the CoV genome is organized as two overlapping open reading frames (ORFs), which encode the replicase genes (ORF1a and ORF1ab), while the remaining 5 to 9 kb contains the genes that encode (i) structural proteins common to all CoVs, including spike (S), envelope (E), matrix (M), and nucleocapsid (N) proteins, and (ii) accessory ORFs that encode proteins unique to specific virus groups (24). The structural and accessory proteins are encoded by a nested set of coterminal subgenomic mRNAs that are generated by discontinuous transcription of negative strands (1, 21, 39, 40, 42–44, 46, 57), followed by positive-strand synthesis and then translation.

Immediately after entry, the genomic RNA is uncoated, and the translation of ORF1 generates either a ~500-kDa polyprotein (pp1a) from ORF1a or an ~800-kDa polyprotein (pp1ab), which is translated only when the ORF1a stop codon is overridden by a −1 ribosomal frameshift that allows the translation of an ORF1ab fusion protein (5). ORF1ab translation occurs at an approximate frequency of 25 to 30%, which leads to a greater-than-threefold enrichment of proteins translated from pp1a (4). During and after translation, pp1a and pp1ab are

* Corresponding author. Mailing address: 2107 MacGavran-Greenberg, CB#7435, University of North Carolina, Chapel Hill, Chapel Hill, NC 27599. Phone: (919) 966-3895. Fax: (919) 966-0584. E-mail: rbaric@email.unc.edu.

▽ Published ahead of print on 28 March 2007.

processed by three functionally active virally encoded proteinases into active intermediates and eventually ~15 mature proteins (6).

Two distinct types of viral proteinases are required to process the nascent polyprotein into component intermediates and mature proteins. The first type is the Papain-like proteinases (PLP1 and PLP2), which cleave nonstructural proteins (nsp1 to nsp3) cotranslationally (7, 8, 18, 45), resulting in mature proteins nsp1, nsp2, and nsp3 as well as polyproteins nsp4 to 11 and nsp4 to 16. These polyprotein intermediates are then processed both cotranslationally and posttranslationally by the second type, a 3C-like proteinase known as 3CLpro or main proteinase (Mpro) (11). Although the exact order and mechanism of processing of mature proteins from these intermediates are yet to be determined, most of these proteins have been observed in their mature form and colocalize with the viral RNA-dependent RNA polymerase to intracellular double-membrane vesicles, where they form the viral replication complex (16). The current model suggests that larger unprocessed intermediates such as nsp4-10/11 (p150) play a role in early negative-strand synthesis, while positive-strand replication is thought to require mature proteins (41). To date, only nsp2 has been shown to be dispensable for replication (17).

In general, nsp1 and nsp2 have unknown functions, nsp3 contains domains important for transcriptional regulation as well as for PLP1 and PLP2 activity, nsp4 and nsp6 are transmembrane domains that may aid in anchoring the replication complex to double-membrane vesicles, and nsp5 is the 3CLpro. nsp7 to nsp10 are four small proteins of unknown function found at the carboxy-terminal end of pp1a. The structures of nsp7 (34) nsp7-nsp8 (56), nsp9 (13, 52), and nsp10 (22, 51) have been solved, and all four proteins have been implicated in RNA synthesis. nsp7 and nsp8 are predicted to form a hollow cylinder postulated to protect double-stranded RNA during transcription/replication (56), nsp8 has a demonstrated RNA primase activity (20), nsp9 has been shown to bind single-stranded RNA (13, 52), and three studies with nsp10 predict that it interacts with RNA, DNA, and/or other proteins (22, 28, 51). nsp11 is a small ~36-nucleotide (nt) segment located at the 3′ end of ORF1a that encodes a small uncharacterized 12-amino-acid peptide with no defined function. nsp12 is the RNA-dependent RNA polymerase (RdRp), nsp13 contains the helicase activity, and nsp14 to nsp16 are enzymes that may function in RNA processing (48).

Studies with nsp10 have shown that it is a 15-kDa protein of unknown function that has been shown to interact with itself, nsp1, and nsp7 (8). It colocalizes with N to sites of viral replication (3) and is essential for replication (D. Deming et al., unpublished data). nsp10 was first predicted to be a possible growth factor-like molecule, as the concentration of nsp10 increased in response to epidermal growth factor (30); however, there is little homology between nsp10 and any other proteins of known function. Complementation studies using temperature-sensitive mutants in several nsp's of MHV have purported that nsp10, along with nsp4, nsp5, nsp12, nsp14, and nsp16, is essential for the assembly of a functional replication/transcription complex (41). Further characterization of the nsp10 temperature-sensitive mutant TS-LA6 has suggested that nsp10 plays a critical role in negative-strand elongation (41, 47, 54). Recent crystallography studies have revealed the structure of nsp10 of SARS-CoV to be a novel zinc finger protein with two zinc finger domains (22, 51), whereas a second report suggested that the biological unit is a dodecamer that forms a hollow, positively charged cylinder that is thought to be a transcription factor (22, 51).

In this study, we employed a reverse-genetics approach to generate mutants of nsp10 in the context of the entire virus to define the functions of nsp10 in CoV replication/transcription. We show that rescued viruses with mutations in nsp10 globally reduce viral RNA synthesis. Mutations resulting in lethal phenotypes mapped to a central core of nsp10 that is resistant to mutation and verified that the zinc-binding fingers (ZFs), including the surrounding residues to which they hydrogen bond, are critical to nsp10 function and CoV viability. Finally, our study is the first study to demonstrate that mutations in nsp10 may affect the processing of the ORF1a/ORF1ab polyprotein.

MATERIALS AND METHODS

Virus and cells. For this study, we used an infectious clone of MHV-A59 developed by our laboratory, which is comprised of seven fragments maintained in pSMART (Lucigen) or pCR-XL-TopoA (Invitrogen) vectors and was amplified according to previously published protocols (55). Recombinant MHV generated by the infectious clone (wt-icMHV) was used as a control in each experiment. The MHV sequence under GenBank accession number NC_001846 was used for primer and cloning design.

Delayed brain tumor (DBT) cells were maintained at 37°C in minimum essential medium supplemented with 10% fetal clone II (Gibco), 10% tryptose phosphate broth, and gentamicin (0.05 μg/ml)-kanamycin (0.25 μg/ml). Baby hamster kidney (BHK) cells exogenously expressing MHV receptor (MHVr) (BHK-MHVr) were maintained at 37°C in the same medium described above with the addition of geneticin (0.8 mg/ml) to select for cells expressing MHVr.

Bioinformatics analysis and mutant rationale. A multiple sequence alignment generated by the National Center for Biotechnology Information (NCBI) (http://www.ncbi.nlm.nih.gov/genomes/SARS/nsP7.html) was used to map the conserved features of nsp10. Bioinformatic predictions were generated using Prosite (19) to predict conserved protein domains, Predictors of Natural Disordered Regions (38) to determine putative disordered domains, the SMART database (26) to search for similarity signatures, and HMMSearch (12) to analyze potential structurally conserved subunits.

Generating mutants. A full-length molecular clone developed by our laboratory (55) was used to engineer the appropriate mutations in the nsp10 sequence, which is found in the MHV-E fragment (55). Briefly, primers that incorporated type IIS restriction enzyme sites (BbsI) bearing each mutation onto the ends of two amplicons that comprised MHV-E (55) were designed (Table 1). In all cases, the wild-type residue(s) was changed to alanine by altering two positions in each codon. The mutants were generated by PCR, cloned into the Topo-XL vector (Invitrogen), grown up in competent Top10 cells (Invitrogen), screened by restriction digestion, and sequenced to verify that the correct changes were added onto each end. Each amplicon was then digested with BbsI and ligated to form the mutated MHV-E fragment. Full-length E constructs were amplified and purified, and the sequence was verified. For assembling the infectious clone, plasmids incorporating cDNA fragments of MHV-A through MHV-G for wt-icMHV and MHV-A to MHV-D, MHV-F, MHV-G, and the mutated E construct for each mutant were transformed into chemically competent Top10 cells (Invitrogen) by heat shock at 42°C for 2 min and then plated onto Luria Bertani (LB) plates with appropriate selection (kanamycin [25 μg/ml] for Topo-XL and ampicillin [50 μg/ml] for pSMART). Colonies were picked and grown under appropriate selection conditions in 5 ml of LB broth maintained at 28.5°C for 16 to 24 h and then purified and screened by restriction digestion. Larger 20-ml stocks were grown at 28.5°C for 24 h for each of the cDNAs. Purified plasmids were then digested with MluI and BsmBI for MHV-A; BglI and BsmBI for MHV-B and MHV-C; BsmBI for MHV-D, MHV-E, and MHV-F; and SfiI and BsmBI for MHV-G (55). After digestion, fragments were electroporated on an 0.8% agarose gel, and appropriate bands were excised and gel purified using a Qiaex II gel extraction kit (QIAGEN) with modifications (55). Briefly, all fragments were resuspended in 620 μl of QX1 buffer, 11 μl QIAEX II silica gel particles, and 12.5 μl 3 M sodium acetate and eluted in 35 μl of elution buffer heated to 70°C. Purified fragments were ligated overnight at 4°C in a total

TABLE 1. Primers used for engineering nsp10 mutants and RT-PCR

Primer	Sequence (5′–3′)	Sense	Purpose
nsp10-E1S	GAAGACGCGGCAACGTACTTGGATTATATAAAACAG	+	Mutant nsp10-E1
nsp10-E1A	GAAGACGTTGCCGCAGGATCTACAGAAAACGCACAC	−	Mutant nsp10-E1
nsp10-E2S	GAAGACGCGGCAGCTGGCACTGGTATGGCCATTAC	+	Mutant nsp10-E2
nsp10-E2A	GAAGACGCTGCCGCACATAACATCTTAACACAATTAG	−	Mutant nsp10-E2
nsp10-E4S	GAAGACGCGGCAGCGGTTGAACATCCAGATGTTGATG	+	Mutant nsp10-E4
nsp10-E4A	GAAGACGCTGCCGCGCAATATATACAAACGGAAGCACC	−	Mutant nsp10-E4
nsp10-E5S	GAAGACGCGGCACCAGATGTTGATGGATTGTGC	+	Mutant nsp10-E5
nsp10-E5A	GAAGACGGTGCCGCAACACGCGAGCGGCAATATATAC	−	Mutant nsp10-E5
nsp10-E6S	GAAGACGCGGCACCTGTGTCATATGTGTTGACG	+	Mutant nsp10-E6
nsp10-E6A	GAAGACGGTGCCGCTATGCCTAAGGGCACTTGGAC	−	Mutant nsp10-E6
nsp10-E7S	GAAGACGCGGCAGTTTGTCAGGTTTGTGGCTTTTGG	+	Mutant nsp10-E7
nsp10-E7A	GAAGACACTGCCGCCGTCAACACATATGACACAG	−	Mutant nsp10-E7
nsp10-E8S	GAAGACGCGGCAGGTAGCTGTTCCTGTGTAGGC	+	Mutant nsp10-E8
nsp10-E8A	GAAGACCCTGCCGCCCAAAAGCCACAAACCTGAC	−	Mutant nsp10-E8
nsp10-U1S	GAAGACGCAGTTAAGATGTTATGTGACCATGCTGGC	+	Mutant nsp10-U1
nsp10-U1A	GAAGACTTAACTGCATTAGTAACGGGAACTCCACCCTGTTT	−	Mutant nsp10-U1
nsp10-U2S	GAAGACGCAATGGCCATTACTATTAAGCCGGAGGCA	+	Mutant nsp10-U2
nsp10-U2A	GAAGACGCCATTGCAGTGCCAGCATGGTCACATAACATCTT	−	Mutant nsp10-U2
nsp10-U3S	GAAGACGCAATTAAGCCGGAGGCAACCACTAATCAG	+	Mutant nsp10-U3
nsp10-U3A	GAAGACTTAATTGCAATGGCCATACCAGTGCCAGCATGGTC	−	Mutant nsp10-U3
nsp10-U4S	GAAGACGCAGAGGCAACCACTAATCAGGATTCTTAT	+	Mutant nsp10-U4
nsp10-U4A	GAAGACGCCTCTGCCTTAATAGTAATGGCCATACCAGTGCC	−	Mutant nsp10-U4
nsp10-U5S	GAAGACGCAGCTTCCGTTTGTATATATTGCCGCTCG	+	Mutant nsp10-U5
nsp10-U5A	GAAGACGAAGCTGCACCATAAGAATCCTGATTAGTGGTTGC	−	Mutant nsp10-U5
nsp10-U6S	GAAGACGCAACTGGTATGGCCATTACTATTAAGCCG	+	Mutant nsp10-U6
nsp10-U6A	GAAGACCCAGTTGCAGCATGGTCACATAACATCTT	−	Mutant nsp10-U6
nsp10-U7S	GAAGACGCAGGTGGTGCTTCCGTTTGTATATATTGC	+	Mutant nsp10-U7
nsp10-U7A	GAAGACCCACCTGCAGAATCCTGATTAGTGGTTGC	−	Mutant nsp10-U7
nsp10-U8S	GAAGACGCAGGTGCTTCCGTTTGTATATATTGCCGC	+	Mutant nsp10-U8
nsp10-U8A	GAAGACGCACCTGCATAAGAATCCTGATTAGTGGT	−	Mutant nsp10-U8
nsp10-U9S	GAAGACGCAGTTTGTATATATTGCCGCTCGCGTGTT	+	Mutant nsp10-U9
nsp10-U9A	GAAGACCAAACTGCAGCACCACCATAAGAATCCTG	−	Mutant nsp10-U9
nsp10-MS	ACAGGGTGGAGTTCCCGTTA	+	PCR and sequencing nsp10
nsp10-MA	CCTAAGGGCACTTGGACAAA	−	PCR and sequencing nsp10
Sg-N1S	AAGAGTGATTGGCGTCCGTA	+	RT and PCR
Sg-N1A	AGCGCGGTTTACAGAGGAG	−	RT and PCR
N-gene-S	ATGTCTTTTGTTCCTGGGCAAG	+	Northern probe
N-gene-A	GCAGTAATTGCTTCTGCTG	−	Northern probe

reaction mixture volume of ~200 μl. The full-length cDNA was then further purified by chloroform extraction and isopropanol precipitation, transcribed using T7 transcription kit (Ambion), and cotransfected into 8×10^6 BHK-MHVr cells in parallel with the N gene driven by an SP6 promoter and transcribed with an SP6 transcription kit (Ambion). Electroporated BHK cells were poured onto ~2.5×10^5 DBT cells seeded in T75 flasks and incubated at 37°C for 24 to 72 h. Flasks were examined at regular intervals for cytopathic effects (CPEs), and viable mutants were verified by reverse transcriptase PCR (RT-PCR) of subgenomic RNA using primers targeting the leader sequence and the 5′ end of the N gene (Table 1). Plaque-purified viruses were sequenced to confirm that the correct mutations were present in the recombinant virus.

Growth kinetics and RNA analysis. Viral stocks were propagated in DBT cells for each viable mutant, and titers were determined by plaque titration. For growth curve analysis, DBT cells were infected at a multiplicity of infection (MOI) of 0.2 PFU/cell in 60-mm plates with a 1-h adsorption period, followed by three washes with phosphate-buffered saline (PBS). Three milliliters of medium was added to each culture, and the infection was maintained at 37°C. Supernatants were harvested at 2, 4, 8, 12, and 16 h postinfection (p.i.), and titers were determined by plaque titration in DBT cells. For analysis of RNA, cells were infected at an MOI of 1 PFU/cell, and total RNA was harvested at 8 and 12 h in TRIzol reagent (Invitrogen). For Northern blot analysis, 1 μg of total RNA from each mutant and wt-icMHV was separated by gel electrophoresis on a 1% agarose gel, transferred onto a nitrocellulose membrane, and probed with a 300-nt biotinylated RNA probe designed to detect the first ~300 nt of mRNA-7 (N gene) using an Ambion (Austin, TX) Northern kit. Bands were detected using the Bright Star Detection (Ambion) system, and membranes were exposed to film.

Reverse transcription, RT-PCR, and real-time PCR. Viral RNA was reverse transcribed to cDNA using SuperScript III (Invitrogen) with modifications to the protocol as follows. Random hexamers (300 ng) and total RNA (5 μg) were incubated for 10 min at 70°C. The remaining reagents were then added according to the manufacturer's recommendations, and the reaction mixture was incubated at 55°C for 1 h, followed by 20 min at 70°C to deactivate the RT. For RT-PCR, a forward primer in the leader sequence and a reverse primer ~200 nt into the N gene (Table 1) were used to generate a ~220-bp product by PCR.

Quantitative real-time RT-PCR was conducted using Smart Cycler II (Cepheid) with SYBR green (diluted to 0.25×; Cepheid) to detect subgenomic cDNA with primers (7.5 pmol) optimized to detect ~120 nt spanning from the leader sequence to the 5′ end of the N gene (Table 1) or genomic cDNA with primers (7.5 pmol) optimized to detect ~120 nt of ORF1a (Table 1). The cDNA from the RT reaction mixture of each virus was diluted $1{:}10^3$, and 1 μl was used for each reaction mixture, with a total reaction mixture volume of 25 μl. Omnimix beads (Cepheid) containing all reagents except SYBR green, primer, and template were used to standardize the reaction conditions, and template concentrations were normalized by concentrations of the housekeeping gene glyceraldehyde-3-phosphate dehydrogenase (GAPDH). In addition, all products were verified by melting curve analysis.

Statistical methods. Three independent infections for each mutant were analyzed by real-time PCR, and differences in copy numbers for genomic and subgenomic RNAs were tested using the paired *t* test with an α value of 0.05.

Immunoprecipitation analysis. DBT cells were infected at an MOI of 2 PFU/ml for 2 h, at which time the medium was removed and replaced with medium lacking Met-Cys but containing 20 μg/ml of actinomycin D (Sigma) and incubated at 37°C for an additional 2 h. At 4 h p.i., [^{35}S]methionine-cysteine

TABLE 2. Sites targeted for mutagenesis

Mutant	aa position(s)	Conservation	Phenotype	Structural location
nsp10-E1	K24 K25	KK in GII,[a] not in SARS; K25 in most[b]	Viable	N terminus of H2[c]
nsp10-E2	D47 H48	DH in GII, H also in GI[d]	Viable	Loop between H2 and H3
nsp10-E4	R78 S79 R80	R78 strictly conserved,[e] position 80 always +[f]	Lethal	H4 near ZF-1
nsp10-E5	E82 H83	Position 82 mostly[b] −,[f] H83 identical in CoVs	Lethal	ZF-1
nsp10-E6	K104 D105	D strictly conserved	Lethal	Near N terminus of H5
nsp10-E7	H113 D114	Mostly − at position 114, H113 identical in GII	Lethal	C terminus of H5 near ZF-2
nsp10-E8	D123 R124	Conserved in GII, + at position 124 also in SARS	Lethal	C-terminal loop near ZF-2
nsp10-U1	C41	Strictly conserved in CoVs	Viable	Loop between H2 and H3
nsp10-U2	G52	Strictly conserved in CoVs	Viable-D[g]	Loop between B1[h] and B2
nsp10-U3	T56	Strictly conserved in CoVs	Viable	Loop between B1 and B2
nsp10-U4	P59	Variable in CoVs	Viable	B3
nsp10-U5	G70	Strictly conserved in CoVs	Viable-D	H3
nsp10-U6	G50	Strictly conserved in CoVs	Viable-D	Loop between B1 and B2
nsp10-U7	Y68	Conserved aromatic in CoVs	Lethal	H3
nsp10-U8	G69	Strictly conserved in CoVs	Lethal	H3
nsp10-U9	S72	Strictly conserved in CoVs	Lethal	H3

[a] GII, group II CoVs.
[b] Mostly conserved indicates some amino acid conservation but not in every group.
[c] H, α-helix.
[d] GI, group I CoVs.
[e] Strictly conserved means identical.
[f] + indicates positive charge, and − indicates negative charge.
[g] D, debilitated.
[h] B, β-sheet.

(0.08 mCi/ml) was added to the infections, and cells were harvested at 9 h. Radiolabeled cells were washed in 1 ml of PBS and then resuspended in 1 ml of cold ST buffer (200 mM sucrose, 10 mM Tris [pH 7.4]). Next, cells were homogenized by 40 passes through a ball-bearing homogenizer and transferred into fresh tubes. Homogenates were then spun at 6,000 × *g* for 3 min at room temperature, and the supernatant was transferred into ultracentrifuge tubes and spun at 300,000 × *g* for 15 min at 4°C. The supernatant was then transferred into a fresh tube (S100), and the pellet was resuspended in 1 ml of ST buffer (P100). The nuclear pellet was resuspended in 1 ml of ST buffer, and the DNA was sheared by passage 20 times through a 20-gauge needle.

Lysates were boiled for 5 min in sodium dodecyl sulfate (SDS) at a final concentration of 1% and then combined with protein A-Sepharose beads and a 1:200 dilution of anti-nsp10 antibody (VU128) in no-SDS lysis buffer (1% NP-40, 150 mM sodium chloride, 0.5% sodium deoxycholate, and 50 mM Tris [pH 8.0]) supplemented with 1% SDS. After incubation at 4°C for 4 h, beads were pelleted and washed with low-salt lysis buffer (no-SDS lysis buffer plus 150 mM NaCl), followed by high-salt lysis buffer (no-SDS lysis buffer with 1 M NaCl) and a final low-salt wash. After rinsing, 30 ml of 2× SDS loading buffer (8% SDS, 0.2 M Tris [pH 8.8], 4 mM EDTA, 0.1% bromophenol blue, 40% glycerol, 0.5 M dithiothreitol) was added to the pelleted beads and boiled for 5 min prior to electrophoresis of the supernatant on 4 to 12% SDS-polyacrylamide gel electrophoresis (PAGE) gels.

IFA. DBT cells were grown to 60 to 70% confluence on 12-mm glass coverslips and infected with wt-icMHV or each of the viable mutants at an MOI of 5 PFU/cell. At 6.5 h p.i., the medium was aspirated, and the cells were fixed and permeabilized in methanol overnight at −20°C. Cells were rehydrated in PBS for 30 min and blocked in buffer comprised of PBS with 5% bovine serum albumin. All subsequent immunofluorescence assay (IFA) steps were conducted at 25°C in IFA wash buffer comprised of PBS containing 1% bovine serum albumin and 0.05% Nonidet P-40. After blocking, cells were incubated in primary antibody (anti-nsp10 [VU128] diluted 1:200 and anti-N diluted 1:1,000 or anti-M diluted 1:1,000) for 1 h. Cells were then washed in IFA wash buffer three times at 10 min/wash. Next, cells were incubated in secondary antibody (goat anti-rabbit Alexa 488 at a dilution of 1:1,000 and goat anti-mouse Alexa 546 at a dilution of 1:1,000; Molecular Probes) for 45 min. Next, cells were washed three times at 10 min/wash, followed by a final wash of 30 min in PBS. Coverslips were mounted onto slides with Aquapolymount (Polysciences), dried for 1 h, and then visualized by confocal immunofluorescence microscopy using a Zeiss LSM 510 laser scanning confocal microscope at 488 and 543 nm with a final magnification of ×40 with the oil immersion lens. Images were prepared for publication using Adobe Photoshop CS.

Analysis of structure. The crystal structure coordinates of SARS nsp10 (PDB accession number 2FYG) (22) were used as a template to generate a homology model of MHV nsp10, which is a predicted three-dimensional structure of this protein calculated from its sequence homology with SARS-CoV nsp10. Homology models were generated using the program Modeler, version 8.2 (15, 27), with the automodel class. A pairwise alignment was generated using the SARS nsp10 protein database (PDB) file and the MHV homologue sequence (GenBank accession number NP_740615), and five models were generated from each alignment, with the best model selected based on the lowest objective-function score. Corresponding PDB files generated by this program were visualized using the molecular modeling tools MacPyMol (DeLano Scientific) and Chimera (35). In addition, homology models of each of 16 mutants were generated using the same parameters.

RESULTS

Mutation design and rationale. To identify functional domains within MHV nsp10 and determine the roles that nsp10 plays in CoV replication, two different alanine-scanning mutagenesis strategies were devised. The first strategy targeted pairs and triplets of charged amino acids, since charged residues often provide electrostatic surface potential required for the interaction of the protein with other proteins or nucleic acids. These sites may play a crucial role in inter- and intraprotein interactions as well as nucleic acid binding, and these were designated the E-series mutants (Table 2 and Fig. 1).

Bioinformatic methods identified an highly active region from amino acids 50 to 75 that contains multiple predicted protein domains and a disordered region potentially indicative of an interaction domain (Fig. 1 and Table 2). The disordered region was not conserved at the amino acid level; however, the same amino acid positions were predicted by Predictors of

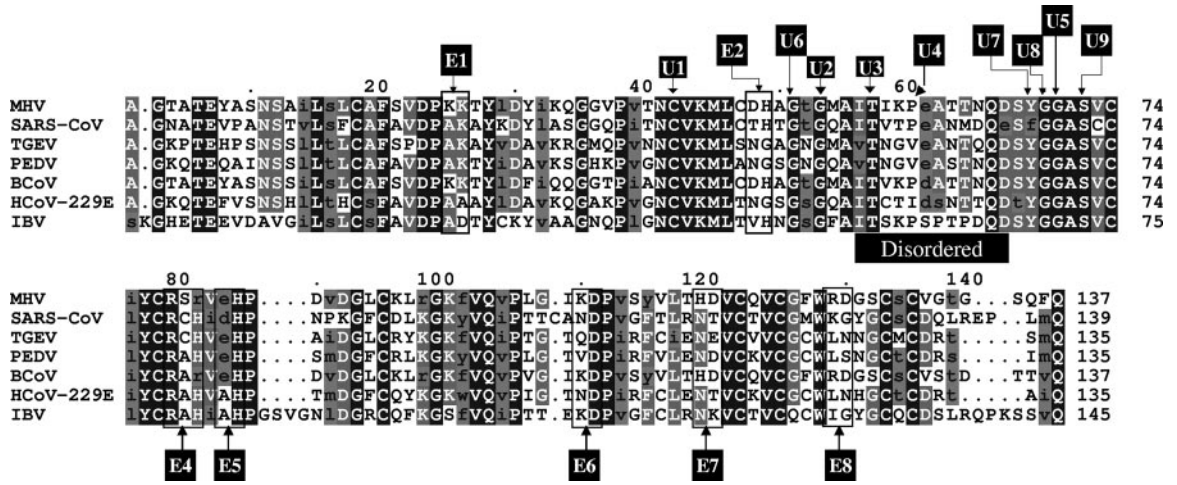

FIG. 1. Mutational design of nsp10 mutants. nsp10 mutants were selected using two approaches. The U series of mutants targeted conserved residues in putative regulatory motifs near a predicted disordered region, and the E-series mutants targeted charged amino acid pairs and triplets. Residues above the black box are predicted to comprise a disordered region. TGEV, transmissible gastroenteritis virus; PEDV, porcine epidemic diarrhea virus; BCoV, bovine CoV; IBV, infectious bronchitis virus.

Natural Disordered Regions (38) to be disordered in all CoVs, indicating that the conserved disordered region may play an important role in nsp10 function. Therefore, the second strategy targeted key residues in this region of nsp10 in an attempt to alter potential protein-protein or protein-nucleic acid interaction sites (Table 2 and Fig. 1) (38) or ablate putative functional domains (myristoylation sites, phosphorylation sites, etc.) (Table 2 and Fig. 1). These mutants were designated the U-series mutants. All U-series mutant amino acids were conserved in nsp10 in all three groups of the *Coronavirus* genus (Fig. 1 and Table 2), except mutant nsp10-U4, which targeted a nonconserved proline present in MHV and SARS-CoV. This change was predicted to add order to the conserved disordered region.

To determine the effects of nsp10 alanine-scanning mutagenesis on MHV replication, the 16 mutations were engineered into the molecular clone of MHV, replacing the wild-type amino acid(s) with alanine. In all cases, two nucleotide changes were made to each codon to reduce the likelihood of reversion to the wild-type sequence. The wild-type fragments of the molecular clone were isolated by restriction endonuclease digestion and ligated with the appropriate sequence-verified mutant fragment, and full-length cDNAs were then transcribed in vitro, transfected into replication-competent cell lines, and monitored for CPE, i.e., syncytium formation (55).

Isolation and genotype of mutant viruses. MHV mutant viruses containing the mutations nsp10-U1, nsp10-U3, nsp10-U4, nsp10-E1, and nsp10-E2 were rescued by 48 h posttransfection and were categorized as the viable mutants. Mutant nsp10-U1 grew with characteristics similar to those of wt-icMHV, with plaque formation and size comparable to those of the wild-type virus. Mutants nsp10-U3 and nsp10-U4 had reduced plaques sizes compared to wt-icMHV. Mutant nsp10-E1 exhibited smaller plaque sizes, with irregular boundaries, whereas viable mutant nsp10-E2 was the most difficult to observe in further analyses due to variably sized plaques with irregular borders and sizes, many of which were much smaller than those of the wild type (~2 mm versus ~5 mm) and barely visible to the eye.

Mutants nsp10-U2, nsp10-U5, and nsp10-U6 exhibited a CPE-negative, RNA positive (CPE^-/RNA^+) phenotype characterized by no detectable CPE in the transfection flask by 48 h posttransfection, although all three generated subgenomic mRNAs at a cycle threshold slightly above the lower limit of detection by real-time PCR (data not shown). However, leader-containing transcripts could not be detected after passage of nsp10-U2 and nsp10-U6. Interestingly, by 72 h posttransfection, nsp10-U5 infections showed signs of CPEs. Sequencing of nsp10-U5 from cells harvested at 48 h posttransfection confirmed the correct mutation (G70A), while sequences generated from infections harvested after 72 h demonstrated a wild-type genotype at the mutant locus. This was repeated with the exact results both times, suggesting that nsp10-U5 reverts to the wild type at two nucleotide positions after 48 h of debilitated replication. Mutants nsp10-E4, nsp10-E5, nsp10-E6, nsp10-E7, nsp10-E8, nsp10-U7, nsp10-U8, and nsp10-U9 were nonviable, as multiple attempts failed to recover virus or detect leader-containing transcripts.

All of the viable mutants nsp10-U1, nsp10-U3, nsp10-U4, nsp10-E1, and nsp10-E2 were plaque purified and sequenced at the nsp10 locus to confirm that the appropriate mutant allele had been incorporated into the molecular clone, and stocks were grown to a high titer for further analyses.

Phenotype analyses. To determine the effects of the nsp10 mutations on viral growth kinetics and global viral RNA synthesis, we compared rescued mutant nsp10 viruses to wt-icMHV via viral growth curves, Northern blot analysis, and quantitative PCR. DBT cells were infected with wild-type or recombinant viruses bearing the viable nsp10 mutations at an MOI of 0.2 PFU/cell for 1 h, and virus growth was assayed over 16 h. All five viable mutants grew to lower titers than did wt-icMHV at all time points up to 16 h p.i. (Fig. 2A). However, nsp10-U1 growth was roughly equivalent to that of the wild-type virus, while the other four mutants displayed lower titers at 8 h p.i.

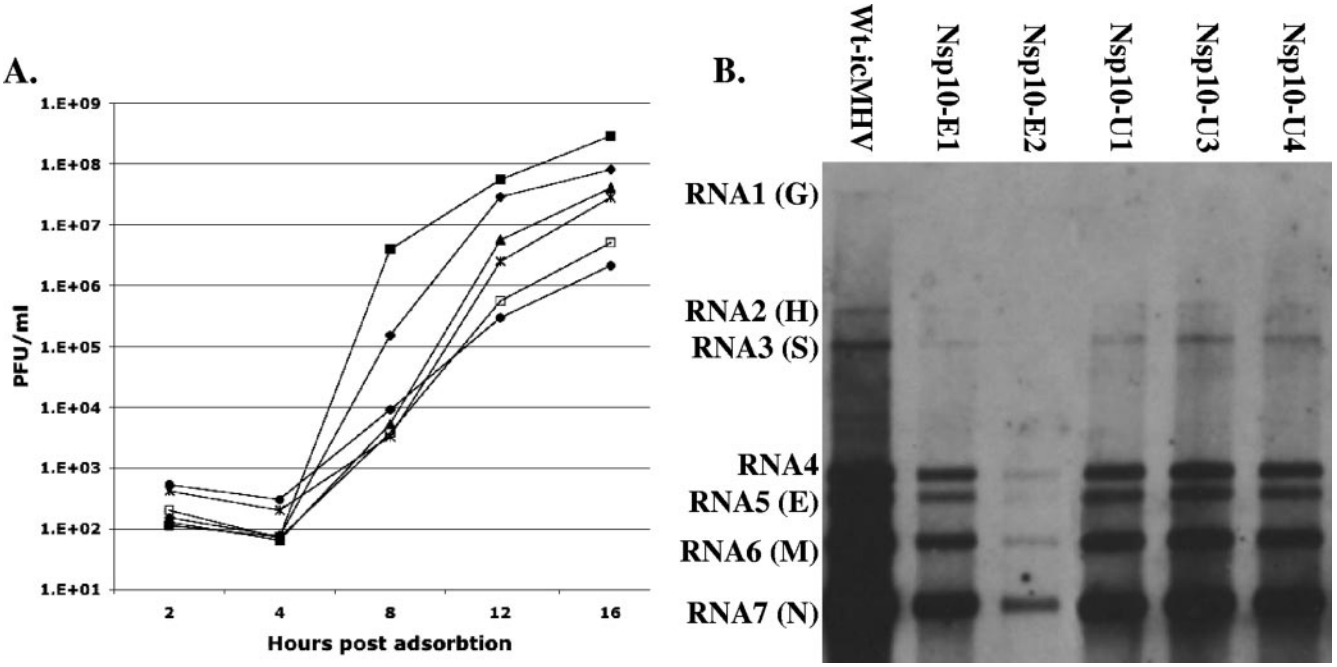

FIG. 2. Growth kinetics and Northern blot analysis of nsp10 mutants. (A) Cultures of DBT cells were infected at an MOI of 0.2 PFU/cell. Virus samples were taken at different time points and measured by plaque assay. All mutants showed reduced growth kinetics at 8 h p.i, while nsp10-U1 recovered by 12 h p.i. to nearly wt-icMHV growth levels. All other viable mutants reached lower titers, with nsp10-U3 and nsp10-U4 showing a 2-log difference at 16 h p.i. Filled square, wt-icMHV; ×, nsp10-E1; filled triangle, nsp10-E2; filled diamond, nsp10-U1; hollow square, nsp10-U3; filled circle, nsp10-U4. (B) Northern blot. Cultures of cells were infected at an MOI of 1 PFU/cell, and intracellular RNA was isolated at 8 h p.i. The RNA was separated on 1% agarose gels, blotted onto a nitrocellulose membrane, and probed with an N-gene-specific probe. The results show that all five mutants have reduced RNA synthesis compared to wt-icMHV, whereas two mutants, nsp10-E1 and nsp10-E2, have reduced subgenomic RNA at 8 h p.i. G, genomic; H, hemagglutinin esterase; S, spike; E, envelope; M, membrane; N, nucleocapsid.

By 12 and 16 h p.i., mutants nsp10-E1 and nsp10-E2 were debilitated, replicating to titers about 1 log lower than those of the wild type, while mutants nsp10-U3 and nsp10-U4 were characterized as having more extensive blocks in virus replication (Fig. 2A). As overall virus growth was reduced for many of the nsp10 mutant viruses, we next evaluated levels of subgenomic viral transcripts using Northern blotting (Fig. 2B) and subgenomic and genomic RNA levels using real-time PCR (Fig. 3B, C, and D).

By Northern blotting, all mutants showed a reduction in subgenomic mRNA synthesis at 8 h p.i., with nsp10-E1, nsp10-E2, and nsp10-U4 showing more extensive blocks in subgenomic mRNA synthesis. nsp10-E2 showed an inordinate reduction in subgenomic mRNA synthesis compared to all other mutants and wt-icMHV at 8 h p.i. (Fig. 2B).

To confirm and extend the Northern blot analysis, real-time PCR was used to quantify viral plus-strand transcripts using primers designed to amplify subgenomic RNA from the N gene or genomic RNA from ORF1a. In agreement with the Northern blot data, quantitative PCR analyses demonstrated that all five mutants were reduced in subgenomic mRNA synthesis at 8 h p.i. compared to wt-icMHV, with more extensive blocks occurring in mutants nsp10-E2, which had a ~900-fold reduction, and nsp10-U4, with a ~60-fold reduction in mRNA synthesis (Fig. 3B and D). All other mutants had reductions of less than 10-fold (Fig. 3D). Analysis of genomic RNA showed the same trend, with reductions in all mutants, while nsp10-E1 showed an approximately 7-fold reduction, nsp10-E2 showed a 900-fold reduction, and nsp10-U4 showed a 17-fold reduction in genomic RNA at 8 h p.i compared to wt-icMHV (Fig. 3C and D). All other mutants were reduced by less than 10-fold (Fig. 3D).

A comparison of the reductions of subgenomic and genomic RNAs at 8 h p.i. demonstrated that mutants nsp10-E2 and nsp10-U1 had equivalent reductions of both genomic and subgenomic RNAs (Fig. 3D). nsp10-E2 had reductions of 900-fold in both genomic and subgenomic RNAs, whereas nsp10-U1 had 2-fold reductions of both (Fig. 3D).

In contrast, nsp10-E1, nsp10-U3, and nsp10-U4 showed differential effects on subgenomic and genomic RNA synthesis (Fig. 3D). nsp10-E1 showed a larger reduction in subgenomic than genomic RNA synthesis, with a 7-fold reduction versus a 3.5-fold reduction, respectively, although this difference was not statistically significant (P value of 0.11). Furthermore, nsp10-U3 and nsp10-U4 demonstrated greater reductions in genomic RNA than subgenomic mRNAs (Fig. 3D). In the case of nsp10-U3, genomic RNA was reduced 3.5-fold, while subgenomic mRNA was reduced only 2-fold, and this difference was statistically significant, with a P value of 0.043. nsp10-U4 also showed a greater decrease in genomic RNAs, with a ~60-fold reduction, versus subgenomic mRNA synthesis, with a ~17-fold reduction (Fig. 3D). This difference was statistically significant, with a P value of 0.024.

However, by 12 h p.i., only steady-state levels of nsp10-E2 RNA were significantly reduced compared to those of wt-icMHV. While nsp10-U4 also displayed slightly reduced levels

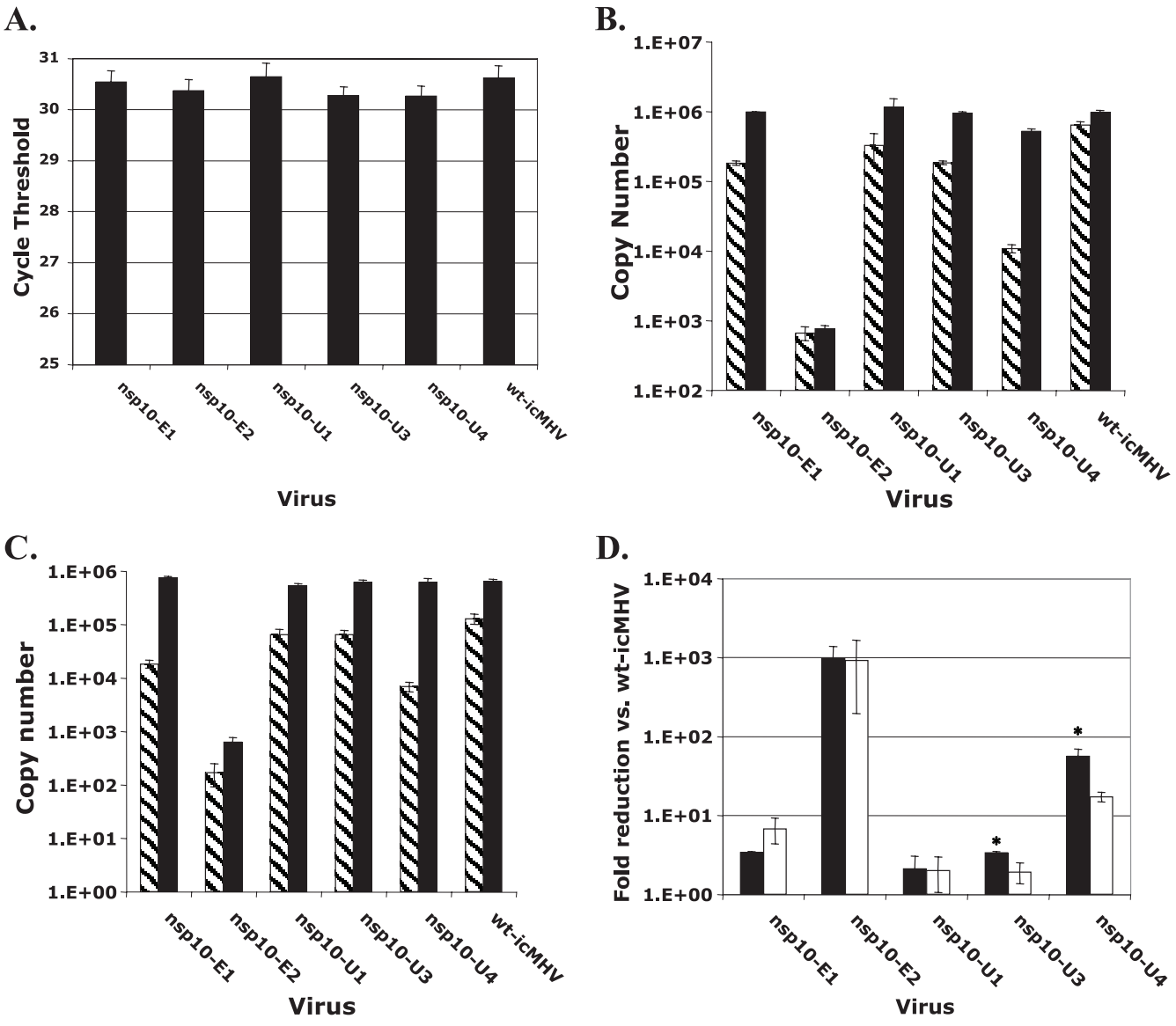

FIG. 3. Real-time PCR analysis of nsp10 mutants. Three independent cultures of DBT cells were infected for each of the nsp10 mutants or wt-icMHV at an MOI of 1 PFU/cell and harvested at 8 and 12 h p.i. Total RNA was isolated, reverse transcribed using random hexamers, and amplified by real-time PCR using primers specific for genomic or subgenomic cDNAs or the housekeeping gene GAPDH. (A) Total RNA for each sample was normalized to GAPDH levels by diluting samples until cycle threshold values, as determined by real-time PCR, were roughly equivalent, indicating equivalent concentrations of starting template. (B) Subgenomic mRNAs for the N gene of wt-icMHV and the viable mutant panel were compared, and in agreement with the Northern blot analysis, all five viable mutants showed decreases in subgenomic mRNA synthesis at 8 h p.i., with a more substantial block occurring in mutant nsp10-E2. However, by 12 h p.i., only nsp10-E2 and nsp10-U4 showed reductions in subgenomic mRNA synthesis. Black-and-white hatched bars, RNA harvested at 8 h p.i.; black bars, RNA harvested at 12 h p.i. (C) Genomic RNA analysis using primers to detect ORF1 cDNA showed that all five mutants were compromised in generating genomic RNA at 8 h p.i., with mutants nsp10-E1, nsp10-E2, and nsp10-U4 exhibiting more extensive blocks in genomic RNA synthesis. Genomic RNA synthesis returned to wild-type levels by 12 h p.i. in all mutants except nsp10-E2. See above for explanation of hatched and black bars. (D) Reductions of subgenomic and genomic RNAs from three independent infections at the 8-h time point were compared and analyzed by the paired *t* test to test the null hypothesis that the reduction in subgenomic mRNAs minus the reduction of genomic RNAs was equal to zero. The null hypothesis was not rejected for mutants nsp10-E2 and nsp10-U1, suggesting that these mutants have an equal reduction in subgenomic and genomic RNAs. The null hypothesis was rejected with *P* values of less than 0.05 for mutants nsp10-U3 and nsp10-U4, suggesting that these mutants are significantly more defective in generating genomic RNAs than subgenomic mRNAs. Mutant nsp10-E1 appears to be more defective in subgenomic mRNA synthesis than in genomic mRNA synthesis, although this difference was not significant (*P* value of 0.110). Black bars, genomic RNA; white bars, subgenomic mRNA; ∗, statistical significance. Error bars represent standard errors with a 95% confidence interval.

of subgenomic RNA compared to those of wt-icMHV, all other mutants had recovered viral RNA synthesis to wt-icMHV levels. nsp10-E2 maintained a ~3-log reduction through both time points.

These results suggest that in general, mutations in nsp10 result in global attenuation of viral RNA synthesis, particularly early in infection. In addition, some mutations demonstrate greater defects in genomic and/or subgenomic mRNA synthe-

sis, suggesting that nsp10 plays a critical role in viral RNA regulation of subgenomic and genomic transcripts.

Replicase protein processing. To assess the impact of nsp10 mutations on polyprotein processing of viral replicase proteins, we performed radiolabeled immunoprecipitations on infected cell lysates to evaluate the processing and expression levels of nsp10. DBT cells were infected with wt-icMHV and the viable nsp10 mutants at an MOI of 2.0 PFU/cell, pretreated with actinomycin D, and switched to Met-Cys-minus medium, and the cultures were labeled with [^{35}S]Cys-Met for 4 h between 8 and 9 h p.i. Cell lysates were fractionated into a crude nuclear pellet and cytoplasmic supernatant. Both the cytoplasmic and nuclear fractions were probed with antibodies directed against nsp10 (VU128), separated on SDS-PAGE gels, and analyzed by autoradiography to detect radiolabeled viral proteins. nsp10 was expressed and processed during infection with each viable nsp10 mutant, although some variation in the amounts of nsp10 was noted among the nsp10 mutant panel (Fig. 4A). For example, mutant nsp10-E2 appeared to express more proteins than all other viruses despite reduced levels of replication and the transcription phenotypes noted above (Fig. 4A).

Current data suggest that nsp4-10/11 is expressed as a polyprotein-processing precursor of ~150 kDa known as p150, which is subsequently processed by 3CLpro via *cis* or *trans* cleavage into the individual replicase proteins (41, 47, 54). The nsp10-E2 mutant contained two novel bands that registered at ~30 kDa and ~71 kDa, respectively. By size analyses, viral precursor polyproteins containing nsp9-11 (29 kDa) and nsp7-11(71 kDa) would be the only appropriately sized intermediates to be immunoprecipitated with anti-nsp10 antisera. These data suggest that the nsp10-E2 mutation may cause subtle changes in nsp4-10/11 polyprotein processing, allowing the visualization of the polyprotein precursor intermediates from the C-terminal end of pp1a.

In addition to cytoplasmic lysates, crude nuclear pellets were also probed with anti-nsp10 antibody (Fig. 4B) to determine if ancillary processing intermediates were detectable. Bands corresponding to nsp10 as well as putative intermediates nsp10-11 (~17 kDa), nsp9-11 (~29 kDa), nsp8-11 (~51 kDa), nsp7-11 (~61 kDa), and nsp6-11 (~92 kDa) were present in crude nuclear lysates from nsp10-E2 (Fig. 4B). In addition to altered processing of the polyprotein, alternate subcellular targeting of mutant nsp10 could account for a reduction in RNA synthesis.

nsp10 replicase protein subcellular localization. To determine if the alanine-scanning mutations in nsp10 altered its subcellular localization, IFAs were performed. Previous studies demonstrated that wild-type nsp10 colocalizes with N to distinct punctuate foci in perinuclear regions that are thought to be the site of the CoV replication complexes (Fig. 5A) (3) and not with M, which localizes to sites of assembly. We probed mock-infected and infected cells with antisera directed against nsp10 and either M- or N-specific antibodies to determine if the panel of nsp10 mutants was targeted to sites of replication similarly to the wild-type protein. The predominant nsp10 signal was localized in perinuclear regions for each of the mutants (data not shown for all mutants) (Fig. 5B). The nsp10 signal was also detected to a lesser extent in the nucleus of DBT cells infected with nsp10-E2 (Fig. 5B) and is consistent with immunoprecipitation data from crude nuclear lysates for nsp10-E2. In all cases, nsp10 mutants appeared to colocalize predominantly to sites of viral replication at 6.5 h p.i. and were not found in sites of particle maturation and assembly.

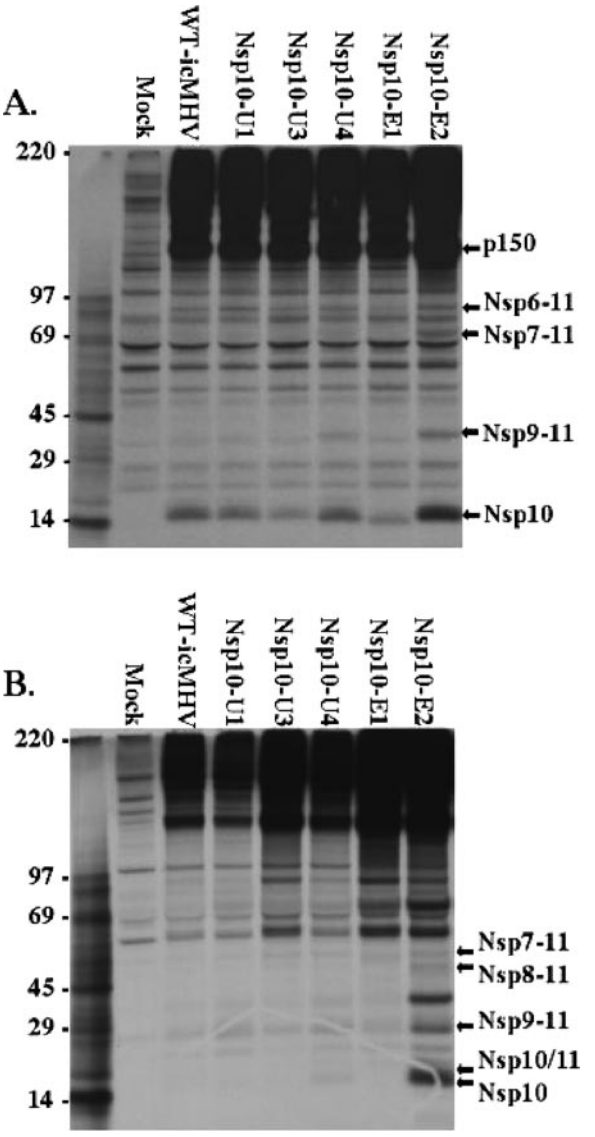

FIG. 4. Immunoprecipitation analysis of nsp10 mutants. Cultures of cells were infected with various mutants, radiolabeled at 4 h p.i. with [^{35}S]methionine-cysteine, and harvested at 9 h p.i. The lysates were immunoprecipitated with anti-nsp10 antibody and separated by SDS-PAGE. (A) Immunoprecipitation analysis of the cytoplasmic lysates showed that nsp10 is expressed and processed in each mutant; however, mutants nsp10-U3 and nsp10-E1 demonstrate a reduction in processed nsp10. In addition, nsp10-E1 shows a reduction in p150. Additional products that are not present in any other virus immunoprecipitated with nsp10-E2. These bands likely represent processing intermediates. (B) The crude nuclear pellet was also immunoprecipitated with anti-nsp10 antibody, and mutant nsp10-E2 shows the accumulation of several novel products, which correspond in size to additional processing intermediates.

Mapping the mutations onto the structure. To identify key residues on the structure of nsp10 that might alter its function, the viable, CPE$^-$/RNA$^+$, and lethal mutants were modeled onto the solved structure of SARS-CoV nsp10. Homology models were generated for wt-icMHV nsp10 and each of the

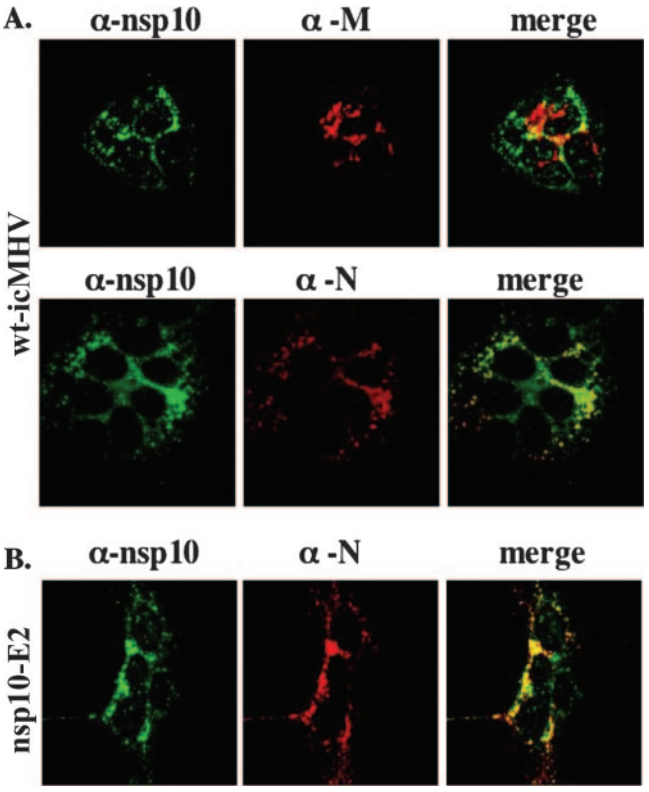

FIG. 5. Confocal IFA of nsp10 mutants. DBT cells were infected with wt-icMHV and the panel of mutants at an MOI of 5 PFU/cell for 6.5 h and fixed in methanol. Cells were then dual labeled with anti-nsp10 (α-nsp10) and anti-N or anti-M to determine if nsp10 colocalizes with N at sites of replication or with M at sites of viral assembly. (A) In wt-icMHV, nsp10 colocalizes with N predominantly to perinuclear foci, where the viral replication complex is thought to assemble. nsp10 clearly does not colocalize with M, a marker for viral assembly. (B) For the panel of mutants, it appeared that nsp10 localized predominantly at the same perinuclear structures as wt-icMHV, with incidental staining occurring in the nucleus in mutant nsp10-E2.

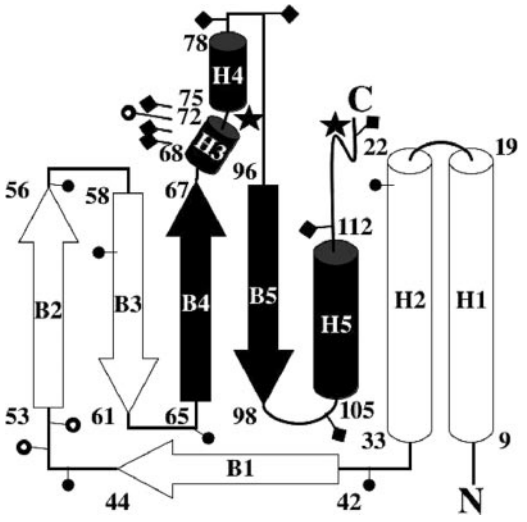

FIG. 6. Topology map of MHV nsp10 showing a conserved core and all 16 mutations. The homology-modeled structure of nsp10 starts with two antiparallel α-helices, α-helices 1 and 2 (H1 and H2), followed by four β-sheets (B1 to B4) and long loops and then two small α-helices, H3 and H4, which are important for ZF-1. After ZF-1, there is another small β-sheet (B5) followed by α-helix 5 (H5) and then ZF-2 at the C-terminal end of nsp10. The central core is colored black, and numbers represent amino acid positions in nsp10 of MHV. Filled circles, viable mutants; filled diamonds, nonviable mutants; hollow circles, CPE^-/RNA^+ mutants; filled stars, ZF-1 and ZF-2. The central core is highly conserved and resistant to mutagenesis, while the loops on either side tolerate mutagenesis.

16 mutants. The backbone of the SARS-CoV nsp10 structure was then compared to the homology model of MHV nsp10 using the MatchMaker tool under the structure comparison section of Chimera (15, 27), resulting in a calculated root mean square distance of 0.207 Å. Each mutant was then analyzed in two contexts: (i) by studying the wild-type residues on the MHV homology model and (ii) by comparing those residues to changes predicted by the homology model for each mutant.

General trends. Joseph et al. solved the SARS nsp10 structure at a resolution of 1.8 Å and reported that it is a single-domain protein comprised of a pair of antiparallel N-terminal helices stacked against an irregular sheet, which contains a coil-rich C terminus, and two ZFs. nsp10 represents a novel fold and is the first structural representative of this family of zinc finger proteins found so far exclusively in CoVs (22, 23).

Mapping of all of the mutations onto the homology model of wild-type MHV provided strong support for both ZFs being essential for nsp10 function and, therefore, MHV replication. In general, the core structure of nsp10 surrounding the ZFs was resistant to mutagenesis, and all mutations in the region were lethal (Fig. 6). This central core, which extends from amino acid 65 through the C-terminal half of nsp10, is also comprised of 27 residues that are identical among all known CoVs and contains both ZFs. Loops that extend away from the central core, for the most part, tolerated mutations resulting in viable phenotypes. The CPE^-/RNA^+ mutants were all glycine-to-alanine replacements that occurred in the outer loops or in H3 (Fig. 6).

DISCUSSION

Previous studies predicted that nsp10 acts as a cofactor in the MHV replication complex (3, 28, 30, 41, 44, 50), which led us to hypothesize that mutations in nsp10 could impact several specific areas of viral RNA synthesis including but not limited to (i) positive-strand synthesis, resulting in reductions of both subgenomic and genomic RNAs; (ii) negative-strand synthesis, resulting in reductions of minus-strand templates; and/or (iii) polyprotein processing, resulting in reductions of essential proteins or intermediates processed from the nascent polyprotein that are essential for the formation of the replication complex. To further examine the functional role of nsp10 in MHV RNA transcription/replication, we applied a reverse-genetics approach incorporating alanine-scanning mutations into the nsp10 gene of the molecular clone of MHV based upon two strategies. First, we hypothesized that conserved regions of nsp10 are essential to its function, so we targeted single residues and a disordered region that are strictly conserved in all CoVs (Fig. 1 and Table 2). Second, we hypothesized that charged residues may provide polar targets on the molecule's surface that facilitate binding to other proteins or nucleic acids; thus, pairs and

triplets of charged amino acids were targeted. In all cases, the targeted amino acid(s) was changed to alanine, as alanine eliminates the side chain beyond the β-carbon but does not alter the main-chain conformation, nor does it impose extreme electrostatic or steric effects (10). Of the 16 full-length mutant viral cDNAs generated, eight constructs resulted in no detectable virus, three generated CPE^-/RNA^+ phenotypes that were lost with passage, and five viruses were rescued with viable phenotypes and further characterized in this study. The high number of nonviable constructs supports previous arguments that nsp10 is essential for CoV replication.

RNA synthesis of each viable mutant was evaluated by analyses of growth kinetics over 16 h and detection of subgenomic versus genomic plus-strand RNA quantities at 8 and 12 h p.i. Growth curve analysis demonstrated that all five viable mutants were compromised in RNA synthesis, with all of them showing reduced growth kinetics compared to those of wt-icMHV (Fig. 2). This trend was confirmed by both Northern blot and real-time PCR, which demonstrated that all five mutants were reduced in RNA synthesis at 8 h p.i., although steady-state levels of RNA became nearly equivalent by 12 h p.i. in all mutants except nsp10-E2 and nsp10-U4. Interestingly, mutant nsp10-E2 showed the largest reduction, with a nearly 3-log reduction in subgenomic and genomic RNA at both time points, while nsp10-U4 showed a more extensive reduction in subgenomic RNA synthesis at the earlier time point.

MHV-A59 is known to produce ~100 subgenomic mRNAs per genomic RNA, and this ratio remains constant throughout the infectious cycle (39), although the ratio of the different subgenomic mRNAs varies greatly, with mRNA-7 (N gene) being the most abundant. In addition, negative strands comprise approximately 1% of the total RNA at any time (41). Mutations that equally reduce subgenomic and genomic RNAs but maintain this ratio would likely introduce a defect in global positive-strand RNA synthesis or a defect in negative-strand template synthesis. In our mutant panel, we observed phenotypes that preserved this ratio as well as those that appeared to alter this ratio with specific reductions in genomic and/or subgenomic RNA synthesis.

Comparisons of the reductions of subgenomic and genomic RNAs for each mutant versus wt-icMHV at 8 h p.i. indicated that mutants nsp10-E1, nsp10-U3, and nsp10-U4 demonstrated differential reductions in subgenomic and genomic RNA synthesis, suggesting that the ratio of subgenomic mRNAs per genomic RNA was altered. In contrast, mutants nsp10-E2 and nsp10-U1 had reductions that were equal in both cases (Fig. 3D), suggesting that RNA synthesis was reduced, but the ratio of subgenomic mRNAs per genomic RNA remained constant at ~100 to 1. However, by 12 h p.i., only nsp10-E2 had subgenomic and genomic RNA levels significantly lower than that of wt-icMHV, with nsp10-U4 genomic RNA synthesis recovering to nearly wild-type levels and subgenomic RNA synthesis recovering to less than a 1-log reduction.

Although it appears that ratios of subgenomic versus genomic RNA eventually recover to wild-type levels by 12 h p.i., differential ratios are evident in mutants nsp10-E1, nsp10-U3, and nsp10-U4 at earlier times of infection. It is worth noting that in similar studies with arterivirus protein nsp11, some mutations produced moderate but significant differences between genomic and subgenomic RNA synthesis (36). This may be occurring at early times of infection in some nsp10 mutants, perhaps due to a defect in negative-strand template synthesis. Alternatively, a mutation that altered the ability of RdRp template switching could reduce subgenomic mRNA quantities and have no affect on genomic minus- or plus-strand synthesis (31, 32). We note that real-time and Northern blot analyses measure accumulated levels of RNA and do not measure the actual rates of subgenomic and genomic mRNA transcription.

These data show that four of five mutants exhibited delays in global RNA synthesis at 8 h p.i. that were overcome by 12 h p.i., whereas nsp10-E2 maintained global ~3-log reductions throughout. There are at least four mechanisms that could account for global reductions of viral RNA synthesis in the nsp10 mutants: (i) a specific defect in negative-strand or global positive-strand synthesis, (ii) a defect in polyprotein processing that impedes the maturation of the replication complex, (iii) a reduction in the molar quantities of processed nsp10 leading to a reduction in the number of functional replication complexes, or (iv) mislocalization of mutated nsp10 proteins to alternative cellular compartments.

Confocal IFA verified that the mislocalization of the mutated forms of nsp10 did not occur, although ancillary staining of nsp10 was detected in the nucleus of cells infected with nsp10-E2 (Fig. 5B). This observation led us to examine viral processing in both the cytoplasmic and nuclear fractions of infected cells.

Operating under the hypothesis that mutations in nsp10 might impede the processing of pp1a/pp1ab by disrupting essential contact sites required for protein-protein *cis* interactions or by interfering with the ability of the polyprotein to fold into a correct orientation to facilitate 3CLpro cleavage, immunoprecipitations were performed to detect nsp10 in the cytoplasmic and nuclear fractions of cells infected with each mutant. In the cytoplasmic fraction, mature forms of nsp10 were processed in each case although at various concentrations (Fig. 4A), whereas in the nuclear fraction, only mutant nsp10-E2 had detectable proteins (Fig. 4B). Interestingly, nsp10-E2 processed novel proteins of 65 kDa and 29 kDa in the cytoplasmic fraction (Fig. 4A), while in the nuclear fraction, proteins of 17 kDa, 29 kDa, 51 kDa, and 65 kDa were detected (Fig. 4B). These novel proteins correlate in mass to putative intermediates nsp7-11 (~65 kDa), nsp8-11 (~51 kDa), nsp9-11 (~29 kDa), and nsp10-11 (~17 kDa) very well.

Although the processing of mature proteins from the nascent polyprotein in MHV-A59 is not completely understood, there is no evidence that these intermediates exist in wild-type or mock infections (Fig. 4A). We hypothesize that nsp10-E2 impedes viral processing of the p150 intermediate, resulting in novel processing intermediates that are either transient or nonexistent in wild-type MHV. These psuedoproforms probably accumulate in excess in the cell and likely aggregate with the membranes pulled down with the crude nuclear pellet, although proteins that are 50 kDa and smaller are capable of inefficiently traversing the nuclear pore complex in the absence of active transport (2). Furthermore, the accumulation of aberrant processing intermediates reduces the number of functional replication complexes, resulting in a global (3-log) reduction of genomic and subgenomic RNAs.

Support for this hypothesis was found in studies with yellow

fever and hepatitis A viruses, which have shown that mutations distant from the polyprotein cleavage site and the active site of the viral protease are capable of reducing proteolytic activity, hypothetically by altering substrate conformation (9, 16). We are currently generating the necessary reagents to verify that these are intermediate forms, to further investigate the fate of the p150 polyprotein during processing in mutant nsp10-E2, and to discern the processing cascade and the exact identity of the intermediates that are present at various times of infection.

Recent structural studies have solved the X-ray crystal structure of SARS-CoV nsp10 and identified a protein with a novel fold containing two ZFs, predicted to be essential to nsp10 function (22, 51). We used the SARS nsp10 crystal structure to generate homology models of MHV nsp10 and then mapped our mutations onto the predicted structure. Of note, mutations responsible for the phenotype of nsp10-E2 (D47A and H48A) removed two charged residues predicted to extend to the surface of nsp10. Removing these side chains appeared to alter the loop region without ablating the nsp10 structure completely. Interestingly, both nsp10-E2 and the known temperature-sensitive mutant TS-LA6 [nsp10(Q65E)] map to the same region on the structure of nsp10, in the loop region proximal to the first ZF. In the case of nsp10-E2, replacing Asp47 and His48 with alanines directly alters the hydrogen bonds Lys43-His48, Asp47-Ala-49, and Asp47-Cys46, which allow the loop to collapse inward, rearranging the surface. Replacing a glutamine with glutamic acid at position 65, as in TS-LA6, adds a negative charge to the surface of the protein and forces the loop to extend outward, probably due to repulsion between Glu65, Asp66, and Glu60, which are in the same proximity. This allows a new hydrogen bond to form between Glu65 and His48, which likely extend the loop outward. TS-LA6 has been characterized as having a defect in negative-strand synthesis (41), and we are currently investigating whether or not TS-LA6 shows a reduction in processing efficiency similar to nsp10-E2.

nsp10-U4 targeted a proline at position 59, which also maps to the same region as nsp10-E2 and TS-LA6. We hypothesized that changing this amino acid to alanine would provide more helical character to this disordered region that is conserved throughout the *Coronavirus* genus. The fact that this mutation conferred differential reductions in genomic and subgenomic RNA synthesis at 8 h p.i. suggests that this disordered region is critical for the regulation of viral RNA synthesis, most likely by interacting with another cofactor or viral RNA. In fact, disordered regions have been implicated as being binding interfaces in other studies (37).

In addition, the mutation to nsp10-U4 might alter the formation of higher-order structures, particularly in conjunction with mutant nsp10-E1. Changing the lysines to alanines in mutant nsp10-E1 (K24A and K25A) removed positive potential from the surface of nsp10, potentially reducing its binding capacity to another cofactor, or viral RNA. In addition, Lys25 has been implicated as being a key aliphatic residue that interacts with Glu60 of a second nsp10 monomer to stabilize the formation of a trimer. Four of these trimers are predicted to interact to form a large dodecamer, which is hypothesized to function as a transcription factor (51). However, replacing Lys25 with alanine would remove the interacting side chain and would likely ablate this interaction site. Additional residues stabilize this interface, and they include Val21 from one monomer that interacts with Val57 and Thr58 of another (51). Mutant nsp10-U4 (P59A) would also likely interfere with this interface at the second interaction site because changing the proline to alanine at position 59 would alter the rotameric positions of neighboring residues 57, 58, and 60, all of which have been predicted to be crucial for trimer formation. The fact that both mutants nsp10-E1 and nsp10-U4 are viable suggests that the dodecamer supercomplex may lack biological relevance. In fact, this structure was solved using the nsp10-nsp11 polyprotein, and experiments in our laboratory have demonstrated that cleavage of nsp11 from nsp10 is essential for replication (Deming et al., unpublished). Although it was shown that nsp11 extends away from the dodecamer (51), it is not known if this supercomplex can form in the absence of nsp11. A second solved structure of nsp10 suggests that nsp10 may form homodimers or homotrimers (22).

Mapping all 16 of our mutations onto the homology model of MHV nsp10 provided important insights into its structure. First, mutations that resulted in lethal phenotypes occurred within or near the ZFs. ZFs are protein domains in which Zn^{2+} contributes to structural stability by binding to residues in the structure to stabilize the domain. There are several classes of ZFs, and these are found in a variety of proteins of diverse function, including proteins involved in the replication and repair of nucleic acids, transcription and translation, cellular signaling and metabolism, and cell proliferation and apoptosis. ZFs most frequently function as interaction sites for the binding of other proteins, nucleic acids, or small molecules (for a recent review, see reference 23). The residues that bind zinc in SARS-CoV nsp10 are strictly conserved throughout the *Coronavirus* genus and include residues Cys74, Cys77, His83, and Cys90, which bind zinc to form ZF-1, and residues Cys117, Cys120, Cys128, and Cys103, which bind zinc to form ZF-2.

The fact the lethal mutations occurred in or near the ZFs indicates that both ZF motifs are critical for infectivity and RNA synthesis in cell culture. Furthermore, in agreement with data reported previously by Joseph et al. and Su et al. (22, 51), our data suggest that the C-terminal half of nsp10 comprises a central core, which spans amino acids 65 to 130 and provides the structure necessary for the formation of both ZFs (Fig. 6). Analyses of the homology models suggest that lethal mutations that mapped within the central core altered the local structural landscape, which prevented the ZFs from forming. We observed three such disruptions. The first disruption, replacement of the essential residues involved in Zn^{2+} binding, as in mutant nsp10-E5 (Q82A and H83A), was lethal. Second, targeting residues that hydrogen bond directly to the four residues that bind Zn^{2+} in both ZFs appears to disrupt the formation of the domain. Lethal mutant nsp10-E4 mutates an Arg78-Ser79-Arg80 motif near ZF-1 in which both arginine residues hydrogen bond directly to the residues that bind Zn^{2+} (Arg78-Cys74 and Arg80-Cys77). Third, altering residues proximal to each ZF probably disrupts the structure enough to prevent ZF formation. Lethal mutants nsp10-E6 (K104A and D105A), nsp10-E7 (H113A and D114A), and nsp10-E8 (R123A and D124A) occur near the ZFs and alter hydrogen bonding. These observations suggest that the structure of the central core is essential for the formation of the ZF domains and provide strong evidence that the ZFs are imperative for nsp10 function.

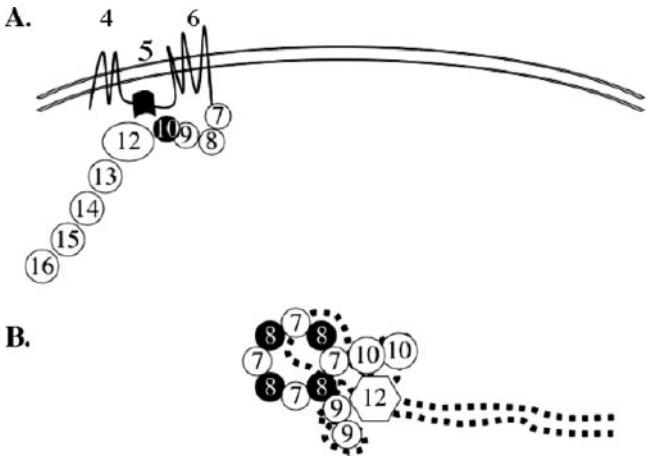

FIG. 7. Pleiotropic roles of nsp10 in CoV replication. (A) After translation, pp1a and pp1ab are processed into precursors and mature proteins. nsp10 appears to influence processing in mutant nsp10-E2, which shows evidence of processing intermediates not seen in wt-icMHV. These data suggest that nsp10 likely interacts with another nsp to facilitate cleavage or maintains a structure that allows the polyprotein to fold into the proper orientation for 3CLpro activation. (B) Once processed, nsp10 functions in replication, probably as a dimer or trimer that binds RNA and nsp7. Our mutant panel suggests that nsp10 may function in both the negative- and positive-strand replicases. The numbers in the diagram represent nsp numbers. The dotted line represents RNA. The curved line represents the double-membrane structure.

The N-terminal region of nsp10, which contains mostly loops that extend away from the structural core of nsp10, tolerated mutagenesis. All of the viable mutants were well away from the ZFs and targeted residues that were not involved in maintaining the local structure necessary for the folding of these domains. However, in all cases, these viable mutations had an impact on viral RNA synthesis, suggesting that nsp10 is a critical regulator of viral RNA synthesis.

The results presented in this paper suggest that nsp10 plays a critical role in the regulation of viral RNA synthesis as well as a potential secondary role in polyprotein processing (Fig. 7A and B). Future experiments designed to measure full-length and subgenomic-length replicative-form RNAs and quantitation of negative strands for each viable mutant will help elucidate the exact role of nsp10 in MHV positive- and negative-strand RNA synthesis. The role of nsp10 in processing is likely by *cis* interactions with a binding partner within the precursor polyprotein. A putative binding site between amino acid positions 48 and 65, which includes the conserved disordered region, may facilitate this interaction. Another possibility is that this region of nsp10 maintains the amino acids necessary for the p150 intermediate to adopt the correct fold to allow other *cis* interactions, which facilitate the autocleavage of the polyprotein by 3CLpro. Pulse-chase experiments have been designed to further examine the fate of the p150 intermediate in nsp10-E2 infection to verify that processing is reduced in that mutant. Additionally, mapping the mutations generating lethal phenotypes onto the structure of nsp10 supports the hypothesis that both ZFs are essential for replication and demonstrates that a conserved central core maintains the functional domain of nsp10.

ACKNOWLEDGMENTS

This work was supported by Research Project grant AI023946 to R.S.B. from the National Institutes of Health (NIH). Data analysis of IFA results was performed in part through the use of the Vanderbilt University Medical Center Cell Imaging Shared Resource (supported by NIH grants CA68485, DK20593, DK58404, HD15052, DK59637, and EY08126).

We gratefully acknowledge the laboratories of Michael Buchmeier and Peter Kuhn and in particular Michael Buchmeier, Benjamin Neuman, Jeremiah Joseph, and Kumar Saikatendu for technical discussions of the nsp10 structure and advice on the use of Modeler. We thank Rhonda Roberts for technical advice regarding statistical analyses. We thank Boyd Yount, Damon Deming, and Will McRoy for technical assistance throughout the project.

REFERENCES

1. **Baric, R. S., K. M. Curtis, and B. Yount.** 2001. MHV subgenomic negative strand function. Adv. Exp. Med. Biol. **494:**459–465.
2. **Bickel, T., and R. Bruinsma.** 2002. The nuclear pore complex mystery and anomalous diffusion in reversible gels. Biophys. J. **83:**3079–3087.
3. **Bost, A. G., R. H. Carnahan, X. T. Lu, and M. R. Denison.** 2000. Four proteins processed from the replicase gene polyprotein of mouse hepatitis virus colocalize in the cell periphery and adjacent to sites of virion assembly. J. Virol. **74:**3379–3387.
4. **Bredenbeek, P. J., C. J. Pachuk, A. F. Noten, J. Charite, W. Luytjes, S. R. Weiss, and W. J. Spaan.** 1990. The primary structure and expression of the second open reading frame of the polymerase gene of the coronavirus MHV-A59; a highly conserved polymerase is expressed by an efficient ribosomal frameshifting mechanism. Nucleic Acids Res. **18:**1825–1832.
5. **Brierley, I., and F. J. Dos Ramos.** 2005. Programmed ribosomal frameshifting in HIV-1 and the SARS-CoV. Virus Res. **119:**29–42.
6. **Brockway, S. M., C. T. Clay, X. T. Lu, and M. R. Denison.** 2003. Characterization of the expression, intracellular localization, and replication complex association of the putative mouse hepatitis virus RNA-dependent RNA polymerase. J. Virol. **77:**10515–10527.
7. **Brockway, S. M., and M. R. Denison.** 2005. Mutagenesis of the murine hepatitis virus nsp1-coding region identifies residues important for protein processing, viral RNA synthesis, and viral replication. Virology **340:**209–223.
8. **Brockway, S. M., X. T. Lu, T. R. Peters, T. S. Dermody, and M. R. Denison.** 2004. Intracellular localization and protein interactions of the gene 1 protein p28 during mouse hepatitis virus replication. J. Virol. **78:**11551–11562.
9. **Chambers, T. J., D. A. Droll, Y. Tang, Y. Liang, V. K. Ganesh, K. H. Murthy, and M. Nickells.** 2005. Yellow fever virus NS2B-NS3 protease: characterization of charged-to-alanine mutant and revertant viruses and analysis of polyprotein cleavage activities. J. Gen. Virol. **86:**1403–1413.
10. **Cunningham, B. C., and J. A. Wells.** 1989. High-resolution epitope mapping of hGH-receptor interactions by alanine-scanning mutagenesis. Science **244:**1081–1085.
11. **Denison, M. R., A. C. Sims, C. A. Gibson, and X. T. Lu.** 1998. Processing of the MHV-A59 gene 1 polyprotein by the 3C-like proteinase. Adv. Exp. Med. Biol. **440:**121–127.
12. **Eddy, S. R.** 1998. Profile hidden Markov models. Bioinformatics **14:**755–763.
13. **Egloff, M. P., F. Ferron, V. Campanacci, S. Longhi, C. Rancurel, H. Dutartre, E. J. Snijder, A. E. Gorbalenya, C. Cambillau, and B. Canard.** 2004. The severe acute respiratory syndrome-coronavirus replicative protein nsp9 is a single-stranded RNA-binding subunit unique in the RNA virus world. Proc. Natl. Acad. Sci. USA **101:**3792–3796.
14. **Enjuanes, L., D. Cavanaugh, K. Holmes, M. Lai, H. Laude, P. Masters, P. Rottier, S. Siddell, W. Spaan, F. Taguchi, and P. Talbot.** 2000. Coronaviridaea, p. 835–859. *In* M. H. V. van Regenmortel, C. A. Fauquet, D. H. L. Bishop, E. B. Carstens, M. K. Estes, S. M. Lemon, J. Maniloff, M. A. Mayo, D. J. McGeoch, C. R. Pringle, and R. B. Wickner (ed.), Virus taxonomy: classification and nomenclature of viruses. Seventh report of the International Committee on Taxonomy of Viruses. Academic Press, San Diego, CA.
15. **Fiser, A., R. K. Do, and A. Sali.** 2000. Modeling of loops in protein structures. Protein Sci. **9:**1753–1773.
16. **Gosert, R., G. Dollenmaier, and M. Weitz.** 1997. Identification of active-site residues in protease 3C of hepatitis A virus by site-directed mutagenesis. J. Virol. **71:**3062–3068.
17. **Graham, R. L., A. C. Sims, S. M. Brockway, R. S. Baric, and M. R. Denison.** 2005. The nsp2 replicase proteins of murine hepatitis virus and severe acute respiratory syndrome coronavirus are dispensable for viral replication. J. Virol. **79:**13399–13411.
18. **Harcourt, B. H., D. Jukneliene, A. Kanjanahaluethai, J. Bechill, K. M. Severson, C. M. Smith, P. A. Rota, and S. C. Baker.** 2004. Identification of severe acute respiratory syndrome coronavirus replicase products and characterization of papain-like protease activity. J. Virol. **78:**13600–13612.
19. **Hulo, N., A. Bairoch, V. Bulliard, L. Cerutti, E. De Castro, P. S. Langendijk-**

Genevaux, M. Pagni, and C. J. Sigrist. 2006. The PROSITE database. Nucleic Acids Res. **34:**D227–D230.
20. **Imbert, I., J. C. Guillemot, J. M. Bourhis, C. Bussetta, B. Coutard, M. P. Egloff, F. Ferron, A. E. Gorbalenya, and B. Canard.** 2006. A second, non-canonical RNA-dependent RNA polymerase in SARS coronavirus. EMBO J. **25:**4933–4942.
21. **Jeong, Y. S., and S. Makino.** 1994. Evidence for coronavirus discontinuous transcription. J. Virol. **68:**2615–2623.
22. **Joseph, J. S., K. S. Saikatendu, V. Subramanian, B. W. Neuman, A. Brooun, M. Griffith, K. Moy, M. K. Yadav, J. Velasquez, M. J. Buchmeier, R. C. Stevens, and P. Kuhn.** 2006. Crystal structure of nonstructural protein 10 from the severe acute respiratory syndrome coronavirus reveals a novel fold with two zinc-binding motifs. J. Virol. **80:**7894–7901.
23. **Krishna, S., I. Majumdar, and N. V. Grishin.** 2003. Structural classification of zinc fingers: survey and summary. Nucleic Acids Res. **31:**532–550.
24. **Lai, M. M., and D. Cavanagh.** 1997. The molecular biology of coronaviruses. Adv. Virus Res. **48:**1–100.
25. **Lau, S. K., P. C. Woo, C. C. Yip, H. Tse, H. W. Tsoi, V. C. Cheng, P. Lee, B. S. Tang, C. H. Cheung, R. A. Lee, L. Y. So, Y. L. Lau, K. H. Chan, and K. Y. Yuen.** 2006. Coronavirus HKU1 and other coronavirus infections in Hong Kong. J. Clin. Microbiol. **44:**2063–2071.
26. **Letunic, I., R. R. Copley, B. Pils, S. Pinkert, J. Schultz, and P. Bork.** 2006. SMART 5: domains in the context of genomes and networks. Nucleic Acids Res. **34:**D257–D260.
27. **Marti-Renom, M. A., A. C. Stuart, A. Fiser, R. Sanchez, F. Melo, and A. Sali.** 2000. Comparative protein structure modeling of genes and genomes. Annu. Rev. Biophys. Biomol. Struct. **29:**291–325.
28. **Matthes, N., J. R. Mesters, B. Coutard, B. Canard, E. J. Snijder, R. Moll, and R. Hilgenfeld.** 2006. The non-structural protein Nsp10 of mouse hepatitis virus binds zinc ions and nucleic acids. FEBS Lett. **580:**4143–4149.
29. **McIntosh, K.** 1974. Coronaviruses: a comparative review. Curr. Top. Microbiol. Immunol. **63:**85–129.
30. **Ng, L. F., and D. X. Liu.** 2002. Membrane association and dimerization of a cysteine-rich, 16-kilodalton polypeptide released from the C-terminal region of the coronavirus infectious bronchitis virus 1a polyprotein. J. Virol. **76:**6257–6267.
31. **Pasternak, A. O., E. van den Born, W. J. Spaan, and E. J. Snijder.** 2001. Sequence requirements for RNA strand transfer during nidovirus discontinuous subgenomic RNA synthesis. EMBO J. **20:**7220–7228.
32. **Pasternak, A. O., E. van den Born, W. J. Spaan, and E. J. Snijder.** 2003. The stability of the duplex between sense and antisense transcription-regulating sequences is a crucial factor in arterivirus subgenomic mRNA synthesis. J. Virol. **77:**1175–1183.
33. **Perlman, S.** 1998. Pathogenesis of coronavirus-induced infections. Review of pathological and immunological aspects. Adv. Exp. Med. Biol. **440:**503–513.
34. **Peti, W., M. A. Johnson, T. Herrmann, B. W. Neuman, M. J. Buchmeier, M. Nelson, J. Joseph, R. Page, R. C. Stevens, P. Kuhn, and K. Wuthrich.** 2005. Structural genomics of the severe acute respiratory syndrome coronavirus: nuclear magnetic resonance structure of the protein nsP7. J. Virol. **79:**12905–12913.
35. **Pettersen, E. F., T. D. Goddard, C. C. Huang, G. S. Couch, D. M. Greenblatt, E. C. Meng, and T. E. Ferrin.** 2004. UCSF Chimera—a visualization system for exploratory research and analysis. J. Comput. Chem. **25:**1605–1612.
36. **Posthuma, C. C., D. D. Nedialkova, J. C. Zevenhoven-Dobbe, J. H. Blokhuis, A. E. Gorbalenya, and E. J. Snijder.** 2006. Site-directed mutagenesis of the nidovirus replicative endoribonuclease NendoU exerts pleiotropic effects on the arterivirus life cycle. J. Virol. **80:**1653–1661.
37. **Romero, P., Z. Obradovic, and A. K. Dunker.** 1997. Sequence data analysis for long disordered regions prediction in the calcineurin family. Genome Inform. Ser. Workshop Genome Inform. **8:**110–124.
38. **Romero, P., Z. Obradovic, and A. K. Dunker.** 2004. Natively disordered proteins: functions and predictions. Appl. Bioinformatics. **3:**105–113.
39. **Sawicki, S. G., and D. L. Sawicki.** 1986. Coronavirus minus-strand RNA synthesis and effect of cycloheximide on coronavirus RNA synthesis. J. Virol. **57:**328–334.
40. **Sawicki, S. G., and D. L. Sawicki.** 1990. Coronavirus transcription: subgenomic mouse hepatitis virus replicative intermediates function in RNA synthesis. J. Virol. **64:**1050–1056.
41. **Sawicki, S. G., D. L. Sawicki, D. Younker, Y. Meyer, V. Thiel, H. Stokes, and S. G. Siddell.** 2005. Functional and genetic analysis of coronavirus replicase-transcriptase proteins. PLoS Pathog. **1:**e39.
42. **Schaad, M. C., and R. S. Baric.** 1993. Evidence for new transcriptional units encoded at the 3′ end of the mouse hepatitis virus genome. Virology **196:**190–198.
43. **Schaad, M. C., and R. S. Baric.** 1994. Genetics of mouse hepatitis virus transcription: evidence that subgenomic negative strands are functional templates. J. Virol. **68:**8169–8179.
44. **Schaad, M. C., W. Chen, S. A. Peel, and R. S. Baric.** 1993. Studies into the mechanism for MHV transcription. Adv. Exp. Med. Biol. **342:**85–90.
45. **Schiller, J. J., A. Kanjanahaluethai, and S. C. Baker.** 1998. Processing of the coronavirus MHV-JHM polymerase polyprotein: identification of precursors and proteolytic products spanning 400 kilodaltons of ORF1a. Virology **242:**288–302.
46. **Sethna, P. B., S. L. Hung, and D. A. Brian.** 1989. Coronavirus subgenomic minus-strand RNAs and the potential for mRNA replicons. Proc. Natl. Acad. Sci. USA **86:**5626–5630.
47. **Siddell, S., D. Sawicki, Y. Meyer, V. Thiel, and S. Sawicki.** 2001. Identification of the mutations responsible for the phenotype of three MHV RNA-negative ts mutants. Adv. Exp. Med. Biol. **494:**453–458.
48. **Snijder, E. J., P. J. Bredenbeek, J. C. Dobbe, V. Thiel, J. Ziebuhr, L. L. Poon, Y. Guan, M. Rozanov, W. J. Spaan, and A. E. Gorbalenya.** 2003. Unique and conserved features of genome and proteome of SARS-coronavirus, an early split-off from the coronavirus group 2 lineage. J. Mol. Biol. **331:**991–1004.
49. **Stadler, K., V. Masignani, M. Eickmann, S. Becker, S. Abrignani, H. D. Klenk, and R. Rappuoli.** 2003. SARS—beginning to understand a new virus. Nat. Rev. Microbiol. **1:**209–218.
50. **Sturman, L. S., C. Eastwood, M. F. Frana, C. Duchala, F. Baker, C. S. Ricard, S. G. Sawicki, and K. V. Holmes.** 1987. Temperature-sensitive mutants of MHV-A59. Adv. Exp. Med. Biol. **218:**159–168.
51. **Su, D., Z. Lou, F. Sun, Y. Zhai, H. Yang, R. Zhang, A. Joachimiak, X. C. Zhang, M. Bartlam, and Z. Rao.** 2006. Dodecamer structure of severe acute respiratory syndrome coronavirus nonstructural protein nsp10. J. Virol. **80:**7902–7908.
52. **Sutton, G., E. Fry, L. Carter, S. Sainsbury, T. Walter, J. Nettleship, N. Berrow, R. Owens, R. Gilbert, A. Davidson, S. Siddell, L. L. Poon, J. Diprose, D. Alderton, M. Walsh, J. M. Grimes, and D. I. Stuart.** 2004. The nsp9 replicase protein of SARS-coronavirus, structure and functional insights. Structure **12:**341–353.
53. **van der Hoek, L., K. Pyrc, and B. Berkhout.** 2006. Human coronavirus NL63, a new respiratory virus. FEMS Microbiol. Rev. **30:**760–773.
54. **Younker, D. R., and S. G. Sawicki.** 1998. Negative strand RNA synthesis by temperature-sensitive mutants of mouse hepatitis virus. Adv. Exp. Med. Biol. **440:**221–226.
55. **Yount, B., M. R. Denison, S. R. Weiss, and R. S. Baric.** 2002. Systematic assembly of a full-length infectious cDNA of mouse hepatitis virus strain A59. J. Virol. **76:**11065–11078.
56. **Zhai, Y., F. Sun, X. Li, H. Pang, X. Xu, M. Bartlam, and Z. Rao.** 2005. Insights into SARS-CoV transcription and replication from the structure of the nsp7-nsp8 hexadecamer. Nat. Struct. Mol. Biol. **12:**980–986.
57. **Zhang, X., C. L. Liao, and M. M. Lai.** 1994. Coronavirus leader RNA regulates and initiates subgenomic mRNA transcription both in *trans* and in *cis*. J. Virol. **68:**4738–4746.